Journal of Materials Chemistry A

ROYAL SOCIETY OF CHEMISTRY

PAPER

View Article Online
View Journal

Cite this: DOI: 10.1039/d5ta08957c

Behind the transduction mechanism of a nanostructured functional material for environmental CO_2 monitoring

A. Rossi, *[a] E. Ghedini, [bc] M. Signoretto, [c] A. Gaiardo, [d] M. Ferroni, [ef] M. Ardit, [g] G. Vola, [h] R. Tassinari,[a] A. Pedrielli, [d] L. Vanzetti,[d] V. Guidi[a] and B. Fabbri [a]

Received 4th November 2025
Accepted 23rd December 2025

DOI: 10.1039/d5ta08957c

rsc.li/materials-a

This work investigated an innovative CO_2-sensitive nanostructured semiconductor material through a three-level approach, *i.e.*, materials and electrical characterization, chemisorption with probe molecules analyses, and *operando* Diffuse Reflectance Infrared Fourier Transform (DRIFT) spectroscopy under thermoactivation. By integrating these advanced techniques, a complete scenario of the sensing mechanism can be obtained, paving the way for the development of highly sensitive and selective CO_2 sensors. It emerged that doping with alkali metals, such as sodium, has proven to be an effective strategy to improve the performance of CO_2 devices. This study presents a sustainable and fast synthesis of three samples with varying sodium content and characterization of each material to explore the role of sodium doping. Therefore, extensive materials characterization confirmed the nanostructured nature of the mesoporous Na-doped In_2O_3 materials as nanoparticles and the presence of intra-structural sodium. These material surfaces were found to possess different acid and basic sites ratio, which can be rationalized by the presence and the amount of sodium. From electrical characterization, a key feature of Na-doped In_2O_3 was the marginal influence of humidity, which enables such sensors to a wide range of possible real-world applications. *Operando* DRIFT spectroscopy clarifies which ones and under what conditions the carbonate species formed upon CO_2 adsorption interact with the material as a function of the presence of acidic and basic sites, a crucial factor influencing the mechanism of transduction. This study uniquely captures the balance of active sites to motivate and explain the optimal sensing behaviour.

1. Introduction

Carbon dioxide (CO_2) emissions are driving global warming and anthropogenic climate change. With current outdoor atmospheric background levels now hovering around 420 ppm, a multifaceted approach to decreasing and monitoring such levels is demanded, which includes research on renewable and green energy sources and the development of reliable, cost-effective, and "smart" CO_2 sensors. Probably less known to the general public, but still more affecting human health is an excess concentration of CO_2 in indoor and confined environments, where people spend most of their time (90%). Here, CO_2 often reaches substantially higher levels than outdoor concentrations.[1] Indeed, indoor CO_2 concentration quantifies an indicator for indoor air quality (IAQ), for the need for air-flow exchange in case there is not sufficient fresh air within confined spaces in buildings.[2] CO_2 concentration is regarded as tolerable up to 800–1000 ppm.[1] Beyond this threshold, fall in cerebral attention, signs of drowsiness, and more generally of environmental discomfort take place. At highest concentrations (>2500 ppm) — especially for prolonged exposures — various health issues, including reduced cognitive function and Sick Building Syndrome[3] commence. Thereby, the need for CO_2 monitoring in both outdoor and indoor contexts becomes impelling. Naturally, an extensive and capillary detection network must rely on compact, inexpensive and low-power-consuming devices, assisted by an Internet of Things (IoT) platform.

A straightforward solution would be the usage of a solid-state chemoresistive sensor owing to high sensitivity, rapid response, stability, and reproducibility combining simple and low-cost

[a]Department of Physics and Earth Sciences, University of Ferrara, Via Saragat 1, Ferrara 44122, Italy. E-mail: arianna.rossi@unife.it
[b]Department of Chemistry, University of Bari, Scientific Campus, Via E. Orabona 4, Bari, Italy
[c]Department of Molecular Sciences and Nanosystems, Ca' Foscari University of Venice, Via Torino 155, 30170 Venezia Mestre, Italy
[d]MTSD-Materials and Topologies for Sensors and Devices, Sensors and Devices Center, Bruno Kessler Foundation, Via Sommarive 18, Trento 38123, Italy
[e]Institute for the Study of Nanostructured Materials CNR-ISMN, Via Gobetti 101, Bologna 40129, Italy
[f]Department of Civil, Environmental, Architectural Engineering and Mathematics (DICATAM) Università degli Studi di Brescia, Via Branze 43, Brescia 25123, Italy
[g]Department of Geosciences, University of Padova, Via G. Gradenigo 6, Padova, Italy
[h]Cimprogetti S.r.l. Lime Technologies, Via Pasubio, Bergamo 24044, Italy

production. In this study, we propose a metal-oxide (MOX) sensor for CO_2 detection over a wide range of concentration (250–5000 ppm). Such devices could be an alternative to commercially available optical devices, such as non-dispersive infrared gas sensors (NDIR). However, the inherent chemical stability of CO_2 molecules makes its transduction difficult as witnessed by the scarce literature with this regard. Among the wide palette of MOX material for gas sensing,[4] indium oxide (In_2O_3) would represent an interesting candidate because it proved to be an efficient catalyst for hydrogenation of CO_2 to methanol.[5] A widely used approach for improving the sensing performance involves the use of dopants to modify their electronic and surface properties. Possibly material synthesis should be carried out *via* sustainable routes. With this perspective, alkali metal doping, in particular with sodium, has shown promise in improving the sensitivity of MOX sensors towards CO_2. In particular, a recent study demonstrated the synergistic effect of sodium and In_2O_3, significantly improving sensing material performance through the use of sodium-doped indium oxide (Na:In_2O_3).[6]

Despite the successful exploitation of these devices—such as monitoring CO_2 concentrations in academic classrooms[1]—a comprehensive understanding of the surface sensing mechanism remains a crucial, limiting factor for advanced material development and performance optimization. Conventional analytical approaches have proven insufficient for establishing the definitive structure–activity relationship.

Indeed, current models of general MOX materials for CO_2 interactions, as outlined in recent studies,[7,8] predominantly emphasize the essential surface chemistry and the spectroscopic characterization of carbonate species (including monodentate, bidentate, or bicarbonate) in relation to temperature or site strength. These studies, however, are typically limited to pure materials (*e.g.*, TiO_2, Y_2O_3, and ZrO_2) and do not transduce these insights directly to the operational sensing mechanism of a device. Other works focusing on sensing applications, *e.g.*, on La_2CO_3 (ref. 9) successfully demonstrate CO_2 detection *via* Diffuse Reflectance Infrared Fourier Transform (DRIFT) spectroscopy but often lack the detailed chemical resolution to distinguish between specific carbonate species or to map their formation to the underlying acidic and basic site chemistry.

Therefore, this work aims to elevate the mechanistic investigation through a robust three-level characterization approach, paying particular attention to the catalytic role of sodium, which boosted the sensor performance.

For this purpose, techniques eminently used in catalysis, such as Temperature Programmed Desorption (TPD) and Temperature Programmed Reduction (TPR) were performed to assess the acidic or basicity nature and strength of surface reaction sites and how they were affected by Na.[10,11] Finally, the mechanism of chemical reactions taking place at surface was investigated through DRIFT spectroscopy, conducted while the sensor was in operation, *i.e.*, in *operando* mode.

The combination of the above techniques allowed one to model the reaction behind sensing mechanism, to identify the role of sodium, and ultimately to dissect the way that functional groups anchor the surface for CO_2 chemisorption.

2. Results and discussion

X-Ray Diffraction (XRD) pattern of the functionalized powders reveals that both pristine and Na-doped samples were monophasic with cubic crystal structure (s.g. Ia-3) (Fig. 1a–d) while the absence of additional phases confirmed that introduction of Na^+ cations did not change the In_2O_3 lattice structure. Incorporation of sodium in the In_2O_3 lattice is supported by the increase in unit–cell parameters proportionally to its content (Fig. S1, in the SI). It can be observed that addition of sodium yielded a crystalline structure that has nearly the same crystallite size (X_{XRD}) but a lower microstrain (e_0) as compared to pure In_2O_3 (see Table 1). This evidence is expected in the case of substitutional Na for In in the In_2O_3 octahedral site because of the larger ionic radius of Na^+ (1.02 Å) than that of In^{3+} (0.8 Å) in octahedral coordination.[12] In summary, Na is very likely incorporated into the In_2O_3 lattice substitutionally. The morphology of In_2O_3-based powders was investigated by Scanning Electron Microscopy (SEM) and Transmission Electron Microscopy (TEM) analyses (Fig. S2). SEM images confirm that the powders consisted of monodisperse nanoparticles and averaged 10–20 nm, with no aggregation phase. High Resolution Transmission Electron Microscopy (HR-TEM) showed regular nanometric spherical particles with an equiaxed shape. The morphologies of the grains in Fig. 1e–h for samples 0.4 and 0.5Na:In_2O_3 look cubic-like while the other two, *i.e.* pristine one and 0.7Na:In_2O_3, take the shape of spheroids. Scanning Transmission Electron Microscopy combined with Energy-Dispersive X-ray (STEM-EDX) analysis confirmed the localization of Na within nanometric In_2O_3 particles (Fig. S3). In particular, to quantify the sodium content in the doped samples, Inductively Coupled Plasma Mass Spectroscopy (ICP-MS) measurements were performed. As shown in Table S1, sodium concentration increased with the amount of sodium used during chemical synthesis.

The presence of sodium was also confirmed by X-ray Photoelectron Spectroscopy (XPS) investigations, which highlighted the nature of its chemical neighbourhood. The survey spectrum of high-resolution XPS on the powders revealed the presence of four main elements, *i.e.* In, O, Na, and C (this latter probably due to carbon impurities). To investigate the chemical state of the main elements, the high-resolution spectra of In 3d (440–455 eV), O 1s (526–535 eV), and Na 1s (1066–1075 eV) core levels were collected. Their quantification (atomic%) in the pristine and doped samples is reported in Table S2. The 0.4Na:In_2O_3 exhibited higher sodium concentration at the surface, around 8.400 at%. Fig. 2a compares the XPS spectrum of the In 3d core level for the powders with and without Na, which clearly shows the doublet corresponding to $3d_{5/2}$ and $3d_{3/2}$. For the pristine In_2O_3 sample, In $3d_{5/2}$ and In $3d_{3/2}$ peaks appeared at 444.1 and 451.6 eV, respectively. The energy of the In 3d doublet corresponds to the In^{3+} oxidation state and In–O bonds. A slight change in the binding energies of the In 3d peaks was observed between pristine In_2O_3 and Na-doped samples. The displacement of these peaks indicates different chemical neighbourhoods due to the incorporation of sodium

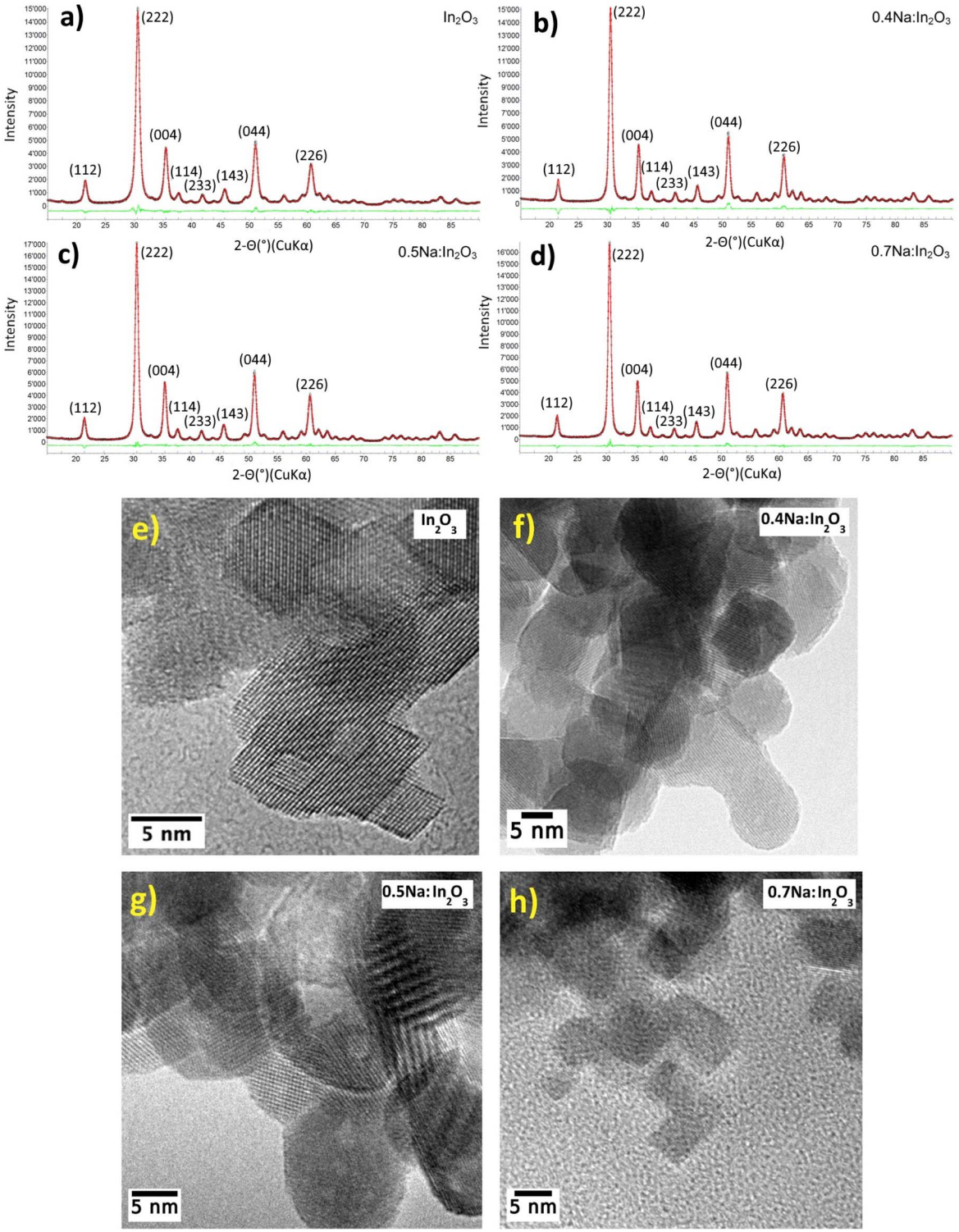

Fig. 1 Rietveld refinement plots of powder diffraction pattern for (a) pure In_2O_3 sample and (b–d) those doped with Na. The experimental profile is represented by black dots, and the best-fit refinement profile is the continuous red line. The lower green curve is the weighted difference between observed and calculated patterns. Vertical ticks mark the position of reflections for the In_2O_3 cubic phase. HR-TEM images of (e) In_2O_3, (f) 0.4Na:In_2O_3, (g) 0.5Na:In_2O_3, and (h) 0.7Na:In_2O_3 powders.

into the In_2O_3 lattice. In addition, for both Na-doped and In_2O_3 powders, Fig. 2b illustrates the deconvolution of O 1s high-resolution spectra in three peaks, corresponding to the O lattice (In–O–In) and surface hydroxyl groups HO–In. The main O 1s peak around 529.6 eV for In_2O_3 (around 529.2 eV for Na-doped powders) corresponds to the O lattice. Binding energies at 531.4 eV for In_2O_3 (average around 531.0 eV for Na-doped samples) are ascribed to adsorbed –OH terminations. To

Table 1 Main crystallographic information such as crystal system, space group, lattice parameter (a), volume cell parameter (V), crystallite size (X_{XRD}), and microstrain (e_0) for the investigated powders

Sample	Phase	Space group	a (Å)	V (Å^3)	Crystallite size, X_{XRD} (nm)	Microstrain e_0 x 100
In_2O_3	In_2O_3 (cubic)	Ia-3	10.1193(4)	1036.22(11)	10.4(1)	0.101(2)
0.4Na:In_2O_3	In_2O_3 (cubic)	Ia-3	10.1212(3)	1036.81(08)	11.6(1)	0.021(7)
0.5Na:In_2O_3	In_2O_3 (cubic)	Ia-3	10.1213(2)	1036.85(07)	10.9(1)	0.060(3)
0.7Na:In_2O_3	In_2O_3 (cubic)	Ia-3	10.1215(2)	1036.90(06)	12.1(1)	0.056(2)

deeply investigate the peaks of O 1s of Na-doped powders, a Shirley background was employed using the Pseudo Voigt with coefficients of the Lorentzian 0.25 and Gaussian 0.75. Fig. S4 and Table S3 show the results of the deconvolution of the O 1s high-resolution spectra, in three peaks, corresponding to the O lattice (In–O–In), H_2O–OH (water chemically adsorbed), surface hydroxyl groups HO–In, and H_2O (~533.0 eV). Finally, Fig. 2c presents and confirms the presence of Na, as a cation incorporated in the crystalline structure.

Adsorption and desorption isotherms are shown in Fig. 3. The corresponding N_2-Brunauer–Emmett–Teller (BET) surface area and pore size for Na-doped samples averaged 42.32 $m^2\ g^{-1}$ and 21.48 nm, respectively. The isotherm profile can be classified as type-IV, with a small hysteresis loop in the range of 0.8–1.0 p/p_0, which indicates the presence of a mesoporous structure according to IUPAC classification.[13]

2.1 Active sites evaluation – TPD and TPR analyses

Fig. 4a shows the results of CO_2 TPD measurements on pristine and Na-doped indium samples following CO_2 desorption at two different pre-treatment temperatures, *i.e.*, 150 °C and 300 °C. For the pristine sample, TPD profile indicates a limited presence of basic active sites at the surface. This is evident owing to the absence of significant desorption bands at medium-to-high temperatures, with only a minor peak observed at approximately 450 °C.

On the other hand, according to the literature,[10] addition of In_2O_3 with alkaline promoters improves the interaction with CO_2, and the higher the difference in electronegativity between In and the alkaline species the stronger the interaction with the analyte. TPD measurements performed on Na-doped samples confirm this hypothesis. Indeed, all desorption profiles were characterized by the presence of well-defined desorption bands localized, predominantly, at medium–high temperatures to indicate basic sites of high strength on the surface of the Na-doped powders. All CO_2 TPD profiles depicted in Fig. 4a can be divided into two main regions, *i.e.*, region I (from 0 to 200 °C) and region II (from 400 to 900 °C). The small desorption peak (around 100 °C) in region I can be assigned to physically adsorbed CO_2 while the broad band in the high-temperature region (450–800 °C, region II), is ascribable to the presence of strong basic sites interacting with the analyte, which can be

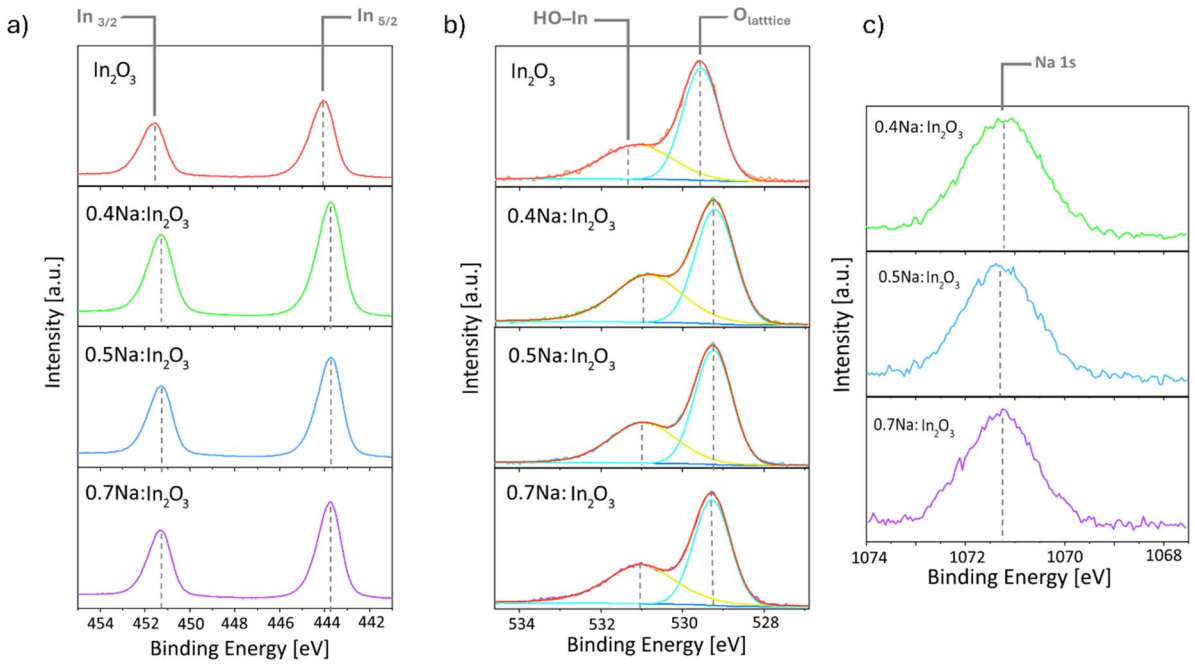

Fig. 2 XPS investigations on 0.4, 0.5, and 0.7Na-doped and pristine In_2O_3 powders. In particular, the figure shows the core-level spectra of (a) In, (b) O, and (c) Na.

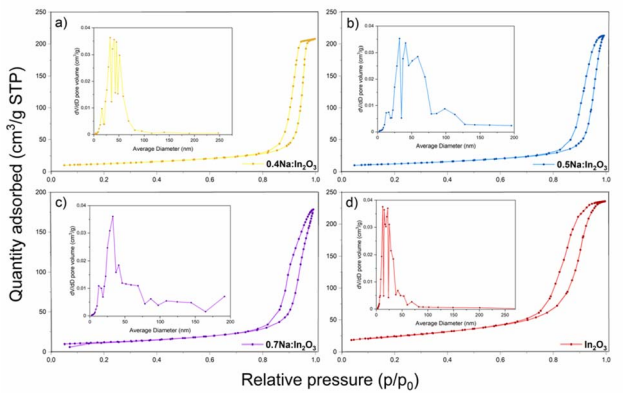

Fig. 3 N_2 isotherm profiles, classified as type-IV, with pore-size distribution in the insets for (a) 0.4Na:In_2O_3, (b) 0.5Na:In_2O_3, (c) 0.7Na:In_2O_3, and (d) pristine In_2O_3 powders.

ascribed with the decomposition of bicarbonate (HCO_3^-) and carbonate (CO_3^{2-}) species.[14] As sodium concentration increases, the desorption bands in the second region moderately shifted to higher temperature and became more evident. As one can observe, the sample doped with the highest sodium amount (0.7Na:In_2O_3), confirmed by ICP-MS, exhibited two defined bands, at 550 and 720 °C, indicating the presence of the strongest adsorption sites. Fig. 4b illustrates the surface acidity of pristine and Na-doped powders, presenting the TPD profiles of ammonia (NH_3) desorption as a function of temperature. The samples were analysed at 300 °C, since no significant desorption bands were observed at room temperature (RT). The low temperature bands (50–200 °C) indicated the desorption of NH_3 from weak acidic sites, most probably Brønsted-type, associated with the –OH groups. In contrast, desorption at temperatures above 400 °C suggested the presence of strong Lewis-type acidic sites, bound to coordinatively unsaturated cations on the MOX surface. In summary, all samples showed amphoteric behaviour. Fig. S5 highlights the result obtained with TPR analyses. In particular, the peak at low temperatures is associated with the reduction of surface Na-doped powders, while the peak at high temperatures could be attributed to the reduction of their bulk. The ease in reduction at low temperatures for doped materials can be correlated to their higher content of oxygen defects.[15] Indeed, a larger concentration of oxygen defects favours the adsorption of CO_2 because the C=O bond can be broken to enable CO_2 adsorption and generation of O radicals. This observation is consistent with recent investigations, showing that several metallic elements (including transition metals, rare earth metals, and alkaline earth metals) have been shown to be effective in generating abundant oxygen defects and improving the catalytic performance.[16]

2.2 Electrical characterization

This section briefly reviews the main characteristics of the films as chemoresistive gas sensors for CO_2 detection.

2.2.1 Optimal working temperature. As shown in Fig. S6, the optimal working temperature for the films, lay in the range 200–250 °C, with a peak at 250 °C. Each film exhibited the highest response at this specific working temperature that maximized its catalytic activity *vs.* CO_2, thus promoting surface redox reactions and the reversible interactions.

2.2.2 Sensitivity. The dynamic response to 1000 ppm of CO_2 in Fig. 5a steadily increased from 2 for In_2O_3 to 11, 8, and 6 for 0.4Na:In_2O_3, 0.5Na:In_2O_3, and 0.7Na:In_2O_3, respectively. These results underscore the extraordinary potential of Na-doped sensors for CO_2 sensing. The calibration curves of the sensors were fitted with an allometric function ($y = a \cdot x^b$), as shown in Fig. 5a with all metric parameters listed in Table S4.

2.2.3 Effect of humidity. As shown in Fig. 5b, the responses *vs.* CO_2 significantly dropped down until 20 RH% while it kept constant beyond this level. In particular, Na-doped In_2O_3 sensors exhibited an important decrease in response (drop ranging from 59% to 75%), whereas pure In_2O_3 nearly vanished. In other words, Na doping renders the sensors more robust *vs.* humidity. In addition, one can observe an increase in the conductance of the sensitive film (insert in Fig. 5b) when the sensor was exposed to 20 RH% with respect to dry conditions (2 RH%), due to homolytic dissociation of water, which reacted

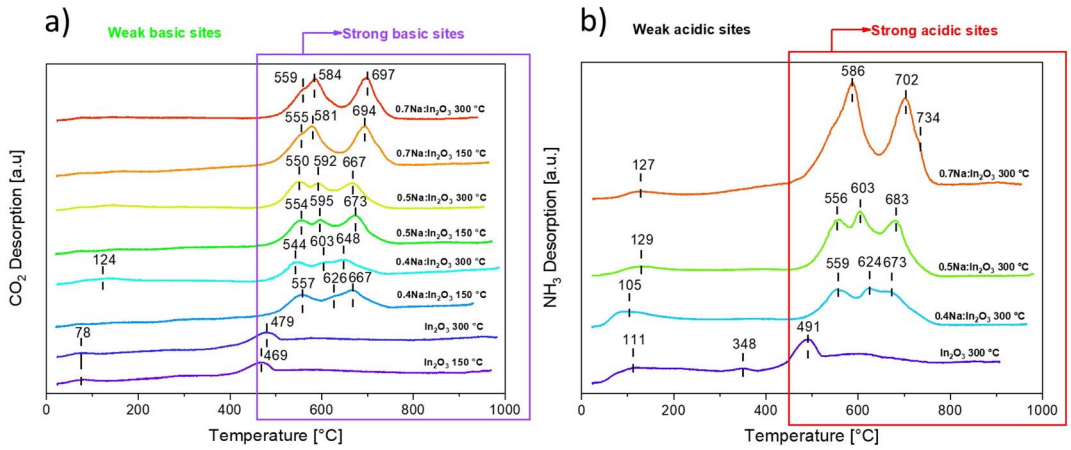

Fig. 4 TPD measurements on pristine and Na-doped powders were carried out with (a) CO_2 and (b) NH_3. TPD analyses with CO_2 were performed on samples pre-treated at 150 and 300 °C, while TPD measurements with NH_3 were performed on powders pre-treated at 300 °C.

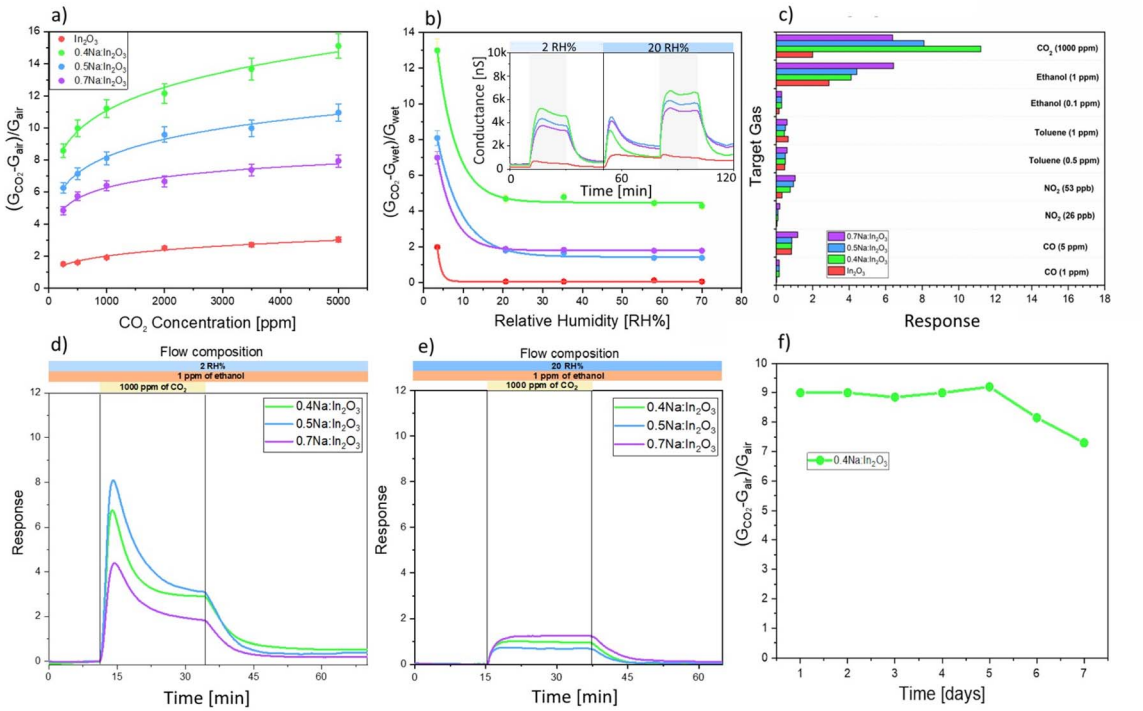

Fig. 5 Electrical characterization of pristine and Na-doped In_2O_3 sensors. The figure illustrates the sensors' key electrical properties: (a) calibration curves, (b) the effect of humidity on sensor response and conductance injecting 1000 ppm of CO_2, (c) selectivity, and (d and e) cross-selectivity with ethanol (1 ppm) and CO_2 (1000 ppm) in dry and humid air. (f) Shows the long-term stability of the sensor over a one-week period with 250 ppm of analyte. The calculated error on the response value is 5%, determined by applying error propagation to account for load resistance tolerance and instrument uncertainty.

with the metal site and a lattice oxygen to form a terminal and a bridged hydroxyl group.[17,18] However, the conductance was only slightly affected by humidity increases above 20 RH%, demonstrating that Na-doped sensors were humidity-independent. In this context, water acted as a surface donor, releasing electrons into the CB. *Operando* DRIFT results presented in the next section will provide an in-depth explanation for the sensing mechanism under dry and wet environments.

2.2.4 Selectivity and cross-selectivity. From Fig. 5c, it turned out that Na-doped sensors showed moderate responses than for pristine In_2O_3 to all the interfering gases tested, *i.e.*, ethanol, carbon monoxide (CO), nitrogen dioxide (NO_2), and toluene, probably due to the high reactivity of such films. In particular, ethanol may represent a common interferent. Therefore, a cross-selectivity test with both ethanol and the analyte were performed under dry and humid environments (Fig. 5d and e). Simultaneous presence of ethanol during exposure to CO_2 marginally affected the response of such devices. The response of 0.4Na:In_2O_3 sensor to 1000 ppm of CO_2 decreased from ~3.5 in dry to ~1 in wet conditions. Instead, the response of 0.5Na:In_2O_3 sensor dropped from ~3.5 in dry to ~0.7 in wet air. Sensor 0.7Na:In_2O_3, on the other hand, showed a less pronounced decrease, ranging from ~2 in dry to ~1.3 under humid conditions. This effect can be attributed to competitive reactions between the reactive gases. Both ethanol and water vapor can interact with active sites on the material, potentially blocking and covering neighbouring active sites.[19] Additionally, reaction products such as chemisorbed alkyl chains can accumulate on the surface, further hindering the accessibility of active sites. However, Na-doped devices demonstrated the effective ability to discriminate against CO_2 in presence of ethanol gas.

2.2.5 Stability. To investigate the stability of the 0.4Na:In_2O_3 film, the most promising from the previous thermo-activated measurements, it was kept at 250 °C under a flux of dry air and every day it was exposed to 250 ppm of CO_2. The measurements were carried out during a period of seven days and are shown in Fig. 5f. The response average remained stable over seven days, with a slight decrease in the last two days. However, the response value remained high, consistent with the expected values based on the calibration.

2.3 *Operando* DRIFT measurements

To elucidate the sensing mechanism that enables analyte sensing, *operando* DRIFT measurements in thermoactivation under dry and wet conditions were performed. This advanced characterization technique provides an insight into the species adsorbed or consumed over the surface, aiding the analysis of the products formed as a result of chemical reactions. The solid–gas kinetics occurring at the surface of In_2O_3–based sensors was investigated by acquiring the *operando* DRIFT spectra at specific intervals of the sensor working, namely during baseline stabilization, transient response, steady state, and baseline recovery. Complete reversibility under exposure to 1000 ppm of CO_2 was inferred (Fig. 6) with the four sensors

working at 250 °C in dry air (2 RH% and 25 °C inside the test chamber). The pristine In_2O_3–based film exhibited an initial resistance of approximately 0.5 kΩ while exposure to 1000 ppm of CO_2 lowered to 0.3 kΩ, resulting in poor response. Instead, the Na-doped films displayed resistances of 3.5 (0.4Na:In_2O_3), 4.2 (0.5Na:In_2O_3), and 4.7 MΩ (0.7Na:In_2O_3), demonstrating an increase in film resistance as sodium concentration was increased. Upon CO_2 injection (1000 ppm), the resistance of all films significantly decreased to 0.5 MΩ. Then, the Na-doped sensors showed a variation in response as a function of dopant concentration, as was shown in the previous section. In particular, 0.4Na:In_2O_3 sensor showed the highest response (13), followed by sensor 0.5Na:In_2O_3 (9) and sensor 0.7Na:In_2O_3 (8.5). In terms of response and recovery times, the devices exhibited 3 min and 9 min (0.4Na:In_2O_3), 5 min and 6 min (0.5Na:In_2O_3), and 11 min and 12 min (0.7Na:In_2O_3), respectively, providing the superior capabilities of 0.4Na:In_2O_3 at the operating temperature of 250 °C. The kinetics of the reaction mechanism are comparable to those reported for other chemoresistive gas sensors based on MOX materials.[20,21] In addition, these times and the low operating temperature (250 °C) represents a good trade-off for CO_2 detection over a wide range of concentrations.

Operando DRIFT spectra (Fig. 6a, c, d, f, g, i, l and n) revealed the presence of hydroxyl groups, *i.e.*, isolated at 3711 cm^{-1} and bridged between 3640 and 3040 cm^{-1} (broadband) adsorbed on the surface during CO_2 feeding (steps 2 and 3), except for the 0.7Na:In_2O_3 sample.[22] These hydroxyl groups probably originated from residual water vapor in the inlet tube or in the gas bottle, which decreased during the recovery to dry conditions (steps 4 and 5). However, gaseous CO_2 molecules and carbonate species built up the highest-intensity peaks in the spectra, especially for doped samples. Indeed, no carbonate species were recorded for pristine In_2O_3 films. On the other hand, the formation of the latter was confirmed by *in-situ* DRIFT spectroscopy on the powder, as shown in Fig. S7, since the use of

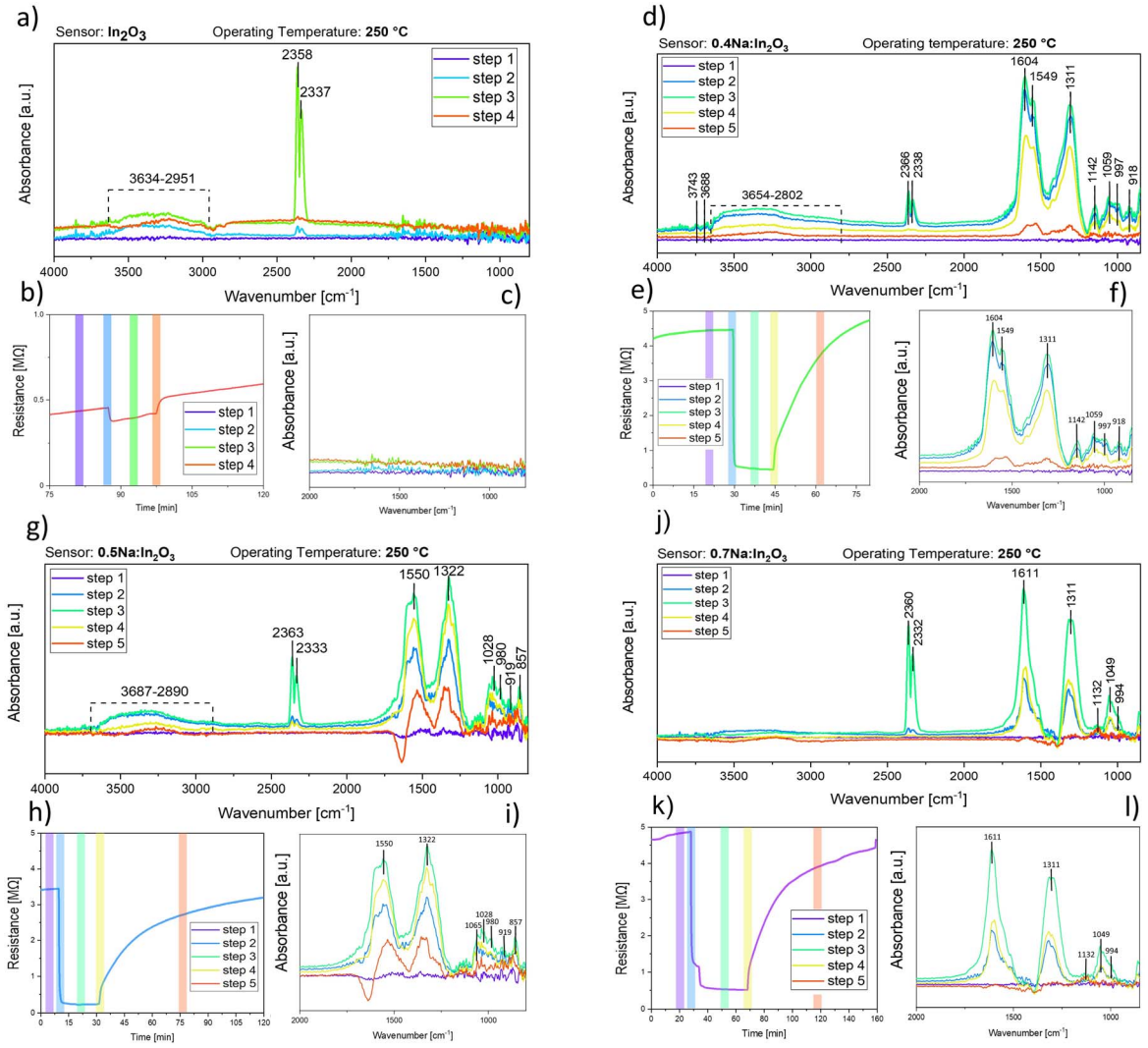

Fig. 6 (a, d, g, and j) DRIFT spectra that are acquired before, during, and after CO_2 injection. (c, f, i, and l) Magnification of the DRIFT spectra in the spectral region between 1000 and 850 cm^{-1}. (b, e, h, and k) Measurements scheme and temporal evolution of sensor resistance during exposure to 1000 ppm CO_2 in dry air at the best operating temperature (250 °C). The coloured bar in these graphs indicates the specific time points at which the corresponding spectra were recorded.

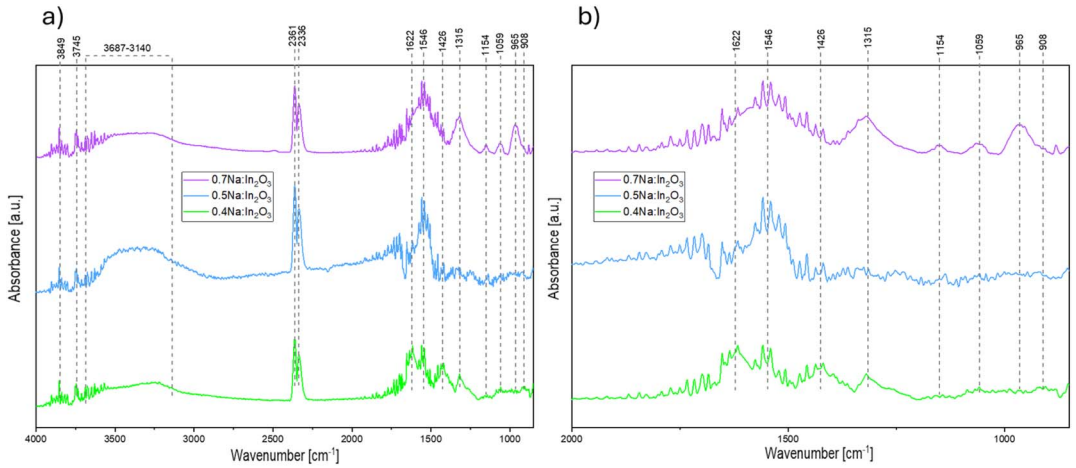

Fig. 7 (a) DRIFT spectra of Na-doped In_2O_3 sensors recorded in the presence of water vapor and 1000 ppm of CO_2. (b) A detailed view of the 2000–800 cm^{-1} region, highlighting the spectral features associated with surface interactions.

a larger spot on functional powders enhances the signal-to-noise ratio allowing to enrich the information obtained by DRIFT on the sensing films. Unlike for doped samples, presence of the characteristic peaks for CO_2 molecules at 2339 and 2365 cm^{-1} and of two main carbonate species within 1600–1200 cm^{-1} regions were acquired (see steps 2 and 3).[9] More specifically, bidentate carbonate (b-CO_3^-) was at 1607 and 1291 cm^{-1} and bridged bidentate carbonate (br-CO_3^{2-}) was at 1564 cm^{-1}.[1,8] Instead, according to Can *et al.*,[23] the bands at 1059 and 1028 cm^{-1} are assigned to In–O lattice vibration.

One can conclude that the decrease in electrical resistance observed upon exposure to 1000 ppm owed to the formation of carbonate species (steps 2 and 3). Conversely, during the recovery phase (steps 4 and 5), film resistance increased as CO_2 was being desorbed, vanishing carbonate species and –OH groups. All sensor characteristics, including material properties, spectroscopic results and electrical behaviour were reported in Table S5.

The behaviour of Na-doped sensors under humidity exposure (22 RH%), was also investigated through *operando* DRIFT technique. Under wet conditions in the presence of 1000 ppm of CO_2 (Fig. 7), the DRIFT spectra can be explained in terms of chemical activity of different types of adsorbates on the surface, *i.e.*, –OH groups, carbonates and bicarbonate species. These latter are generated from the reaction between –OH groups and the analyte. The narrow and intense peaks between 4000–3300 and 2100–1300 cm^{-1}, which increased with the humidity concentrations, are assigned to –OH modes (terminal and interacting).[17] The broad feature below 3500 cm^{-1} can be associated with interacting hydroxyl groups. In particular, despite the results obtained in dry conditions, the 0.4Na-doped In_2O_3 film exhibited the formation of bidentate bicarbonate species at 1426 cm^{-1}. These latter with carbonate species within 1600–1200 cm^{-1} regions can release electrons onto the surface, thereby increasing the material's conductivity. This constitutes a synergistic effect where water plays an active role in the reaction mechanism, rather than simply passivating the surface.

3. Gas sensing mechanism

The gas-sensing mechanisms of Na-doped In_2O_3 films, will be shown to rely on three factors, such as (i) activation of chemisorbed active sites from oxidative and reductive reactions, (ii) creation of acidic or basic centers, and (iii) hydrate–hydroxyl layers, which, synergically combined, play a crucial role to explain the reactivity.

(i) The sensing mechanism can be explained in terms of band-bending theory (Fig. 8a). As mentioned in previous work,[24,25] carried out in dry environment at operating temperature ranging within 100–500 °C, the interaction of the sensing layer with atmospheric oxygen leads to its ionosorption as molecular (O_2^-) and/or atomic (O^- and O^{2-}) species. Accordingly, since the operating temperature of the sensors in present work was 250 °C, pre-adsorbed oxygen species are O^-. As a result, atmospheric oxygen traps electrons from the CB, building up a potential barrier hence increasing the film resistance as compared to RT operation. By exposure to CO_2, such molecules react with pre-adsorbed oxygen ions through eqn (1) and (2), resulting in the formation of carbonate ions with release of electrons in CB. An increase in the concentration of free electrons in CB lowers the potential barrier and then film resistance, too.

$$O_{2(ads)}^- \rightleftharpoons 2O_{(ads)}^- \quad (1)$$

$$CO_2 + O^- \leftrightarrow CO_3 + e^- \quad (2)$$

(ii) Due to their intrinsic basicity and high abundance, alkali and alkaline-earth metals are widely used as promoters to increase the concentration of surface basic sites so as to promote CO_2 adsorption.[16] However, it is important to note that Na-doped In_2O_3 possesses both acidic and basic sites, which further complicates the interaction with the analyte. In particular, CO_2 can be adsorbed or reacted on acid-base materials, resulting in three common forms: (1) carbonate (CO_3^{2-}) formed by reaction with the O sites, (2) bicarbonate (HCO_3^-) formed by

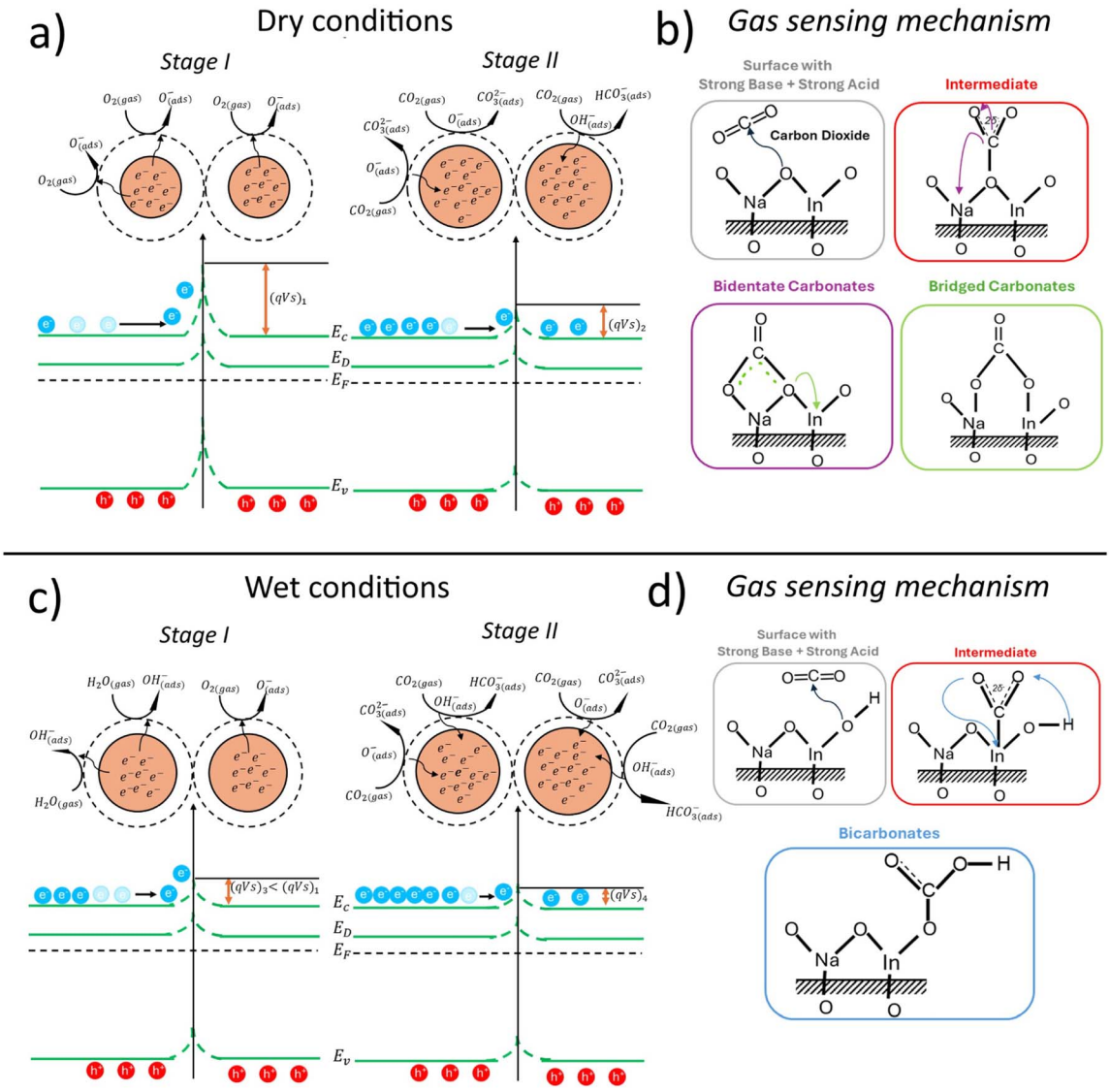

Fig. 8 Sensor mechanism reaction. (a) Surface states in dry air (stage I) *vs.* CO_2 exposure (stage II) and (b) the reaction pathways under analyte injection. (c) Band diagram in wet air (stage I) and under CO_2 exposure (stage II). (d) Gas sensing mechanism under humidity conditions. Symbols E_c and E_v are the conduction and valence bands, E_F is the Fermi level, and E_D is the donor level created due to the doping by Na.

reaction with surface –OH, and (3) adsorption without molecular bending (parallel or perpendicular to the surface). Higher surface acidity can foster adsorption without bending, while more basic metal oxides favour the formation of bent and reactive CO_2^- radical on the surface, due to the electron-donating character of the surface (1 and 3). Forms (1) and (2) can be regarded as the products through such activation on basic sites, mainly consisting of surface oxygen atoms.[26] However, presence of excessively strong basic sites (like Lewis's sites) may excessively retain CO_2, preventing its desorption (release) and ultimately the sensor reversibility. Therefore, the optimal concentration of 0.4 M must be a trade-off between these two counteracting factors. Based on previous characterisations, the 0.4Na:In_2O_3 material, which exhibited best performance *vs.* CO_2 detection, was the optimal choice. The proposed sensing mechanism of these sensors under dry conditions is detailed in Fig. 8b, which illustrates the principal species formed over the surface.

(iii) Under a wet environment, water molecules both interact with and hinder chemisorbed oxygen at the surface and reduce the sensing performance. Indeed, the amphoteric nature of water plays a twofold role. While H_2O molecules can be directly adsorbed on the surface (Lewis's base), they can interact with metal cations (Lewis's acid), forming a strong binding and resulting in their dissociation, then generating –OH groups. In this second case, Lewis acidic cations, *i.e.*, W^{6+}, Sn^{4+}, In^{3+}, and Zn^{2+} (in descending order), can bind –OH groups, then acquire an acidic proton and behave like Brønsted acid sites. This effect leads to an increase in the semiconductor conductance because redox reactions feed electrons into the sensing materials[19] (Fig. 8c). This effect lowers the potential barrier in humid air making the film more conductive than in dry air. Indeed, by exposing the sensor to CO_2 in wet conditions, hydroxyl groups

promote the formation of bicarbonate species, ultimately decreasing the potential barrier (Fig. 8c and d). The presence of humidity is typically seen as a drawback that passivates the sensor surface, competes for the same active sites and reduces response, instead this work demonstrates the opposite. In particular, this study demonstrated that these Na-doped In_2O_3 materials present both acidic and basic sites. As described above, In_2O_3 is classified as a moderately acidic semiconductor which can bind –OH groups and promoted bicarbonates production. On the other hand, due to CO_2 acidic character and its electrophilic nature as a Lewis acid, it preferentially tends to interact with the basic sites[11] and forming carbonates, such as bidentate and bridged species. Therefore, it is highly reasonable that water does not compete with CO_2 for the occupation of the same basic sites. This investigation shows that water plays a crucial, synergistic role in the sensing mechanism itself. By providing an in-depth explanation of water's participation, the study accounts for the remarkable observation that the sensor's performance is maintained also in humid conditions, proving that water actively participates in the reaction instead of simply hindering it.

4. Conclusions

The fundamental novelty of present work consists of a study on CO_2 sensing properties of Na-doped In_2O_3 *vs.* Na content. Such concentration modulated the density and strength of basic sites, thereby promoting CO_2 adsorption. In particular, this study focused on a three-level approach *i.e.*, materials and electrical characterization, chemisorption with probe molecules analyses, and *operando* DRIFT spectroscopy under operating temperature. To understand these aforementioned features, inter- and multi-disciplinary approaches were worked out. The structural, morphological, chemical and elemental, pore volume and surface area, and optical properties of the produced powder nanostructured sodium-doped indium oxide materials were thoroughly examined. Therefore, an extensive characterization by XRD, SEM-TEM, EDX, ICP, BET, XPS, and TPD/TPR confirmed the nanostructured nature of the meso-porous materials as nanoparticles and the presence of sodium dispersed in the crystalline structure, slightly increasing their cell volume. In addition, these material surfaces were found to possess different basicity, which can be rationalized by the presence and the amount of sodium. Then, the sensing performance of such functionalized materials were analysed by an extended electrical characterization by investigating the sensitivity in dry and in humid conditions. A deeper analysis of selectivity, cross-selectivity, stability, and possibility of working at a low operating temperature was addressed. A key feature of Na-doped In_2O_3 was the marginal influence by humidity, which enables such sensors to a wide scenario of possible real-world applications. The sensing mechanism behind CO_2 detection was studied too. *Operando* DRIFT spectroscopy was used for the purpose with the sensor operating under thermal activation. Formation of carbonate species, such as bridged and bidentate carbonates, upon CO_2 adsorption were identified as a key factor influencing the mechanism of transduction. Among the tested Na-doped films, the material with the lowest Na concentration, *i.e.*, 0.4Na:In_2O_3 exhibited superior performance in dry and humid environments with a response rate higher of 35% and 45% at 1000 ppm analyte, respectively, than 0.7Na:In_2O_3. This conclusion was attributed to the amphoteric nature of Na-doped In_2O_3 that features an optimal distribution and presence of both active sites, specifically acidic and basic sites. Considering that both the response and recovery times are less than 10 minutes, this sensor is considered suitable for continuous CO_2 monitoring in real-world applications. Unlike what is often assumed, our findings show that humidity does not reduce sensor performance but rather plays an active and synergistic role in the reaction mechanism. This explains the sensor's consistent and stable response, even in the presence of water vapor. Therefore, this study clarifies which ones and under what conditions the carbonate species formed interact with the material as a function of the presence of acidic and basic sites.

To further investigate this mechanism, it might be necessary to conduct H_2O/D_2O isotope exchange experiments to discriminate the different groups on the surface. Furthermore, to better understand the nature and quantify the active sites in such materials it might be imperative to conduct quantitative TPD and TPR measurements and FT-IR analyses with probe molecules to discriminate the different acidic and basic active sites, *i.e.*, Lewis and Brønsted–Lowry.

5 Experimental section

In this work, three different Na-doped indium oxides were synthesised by means of sol–gel method, as detailed in the following subsection. Morphology, elemental composition, structural, porosity and specific surface area, and specific surface area, active sites of the nanopowders were investigated by X-ray diffraction (XRD), scanning electron microscopy (SEM), high-resolution transmission electron microscopy (HR-TEM), energy-dispersive X-ray (EDX), scanning transmission electron microscopy combined with energy-dispersive X-ray (STEM-EDX), Inductively Coupled Plasma Mass Spectrometry (ICP-MS), N_2 physisorption analysis (Brunauer–Emmett–Teller (BET)), Temperature-Programmed Desorption (TPD) with probe molecules, and Temperature-Programmed Reduction (TPR) analyses. The effect of sodium incorporation in the indium oxide nanostructure was derived from the optical properties obtained by X-ray photoelectron spectroscopy (XPS). Then, sensing devices were produced by a scalable and controllable fabrication technique such as screen printing. The sensors based on pristine and Na-doped indium oxide were electrically characterized to probe their sensing performance *vs.* operating temperature. Finally, the impact of sodium addition on sensing was investigated using *operando* and *in situ* DRIFT spectroscopy under operational conditions in dry and wet conditions. All specifications about the instruments, equipment, data collection, and their setting up are reported in the SI.

5.1 Powder synthesis and gas sensors fabrication

According to recent work by Rossi *et al.*,[6] powder synthesis was carried out through sol–gel method. In this study, the range of sodium concentration was extended with the aim of

performance optimization. Here, three different samples were synthesized in powders through the sol–gel approach, by varying the sodium content. Firstly, 0.1 M of $In(NO_3)_3 \cdot 5H_2O$ (Sigma-Aldrich, 99.9% trace metals basis) was dissolved in 60 mL of distilled water (DI). Secondly, 0.4, 0.5, and 0.7 M of NaOH were added to the above precursor aqueous solution and stirred for 40 min at 70 °C. Specifically, the In : Na molar ratio was 1 : 4, 1 : 5 and 1 : 7, and the sensors labels were 0.4Na:In_2O_3, 0.5Na:In_2O_3, and 0.7Na:In_2O_3 respectively. The slurries, obtained from the three syntheses, were washed with isopropanol and DI water several times using a centrifuge at 5000 rpm for 2 min. The white precipitates were dried at 150 °C for 3 h and consecutively at 250 °C for 2 h. The dried powders were thermally treated at 450 °C for 3 h in ambient air. Then, the powders were mixed with organic excipients, *i.e.*, α-terpineol, ethyl cellulose, and silica, to form a homogeneous paste. The role of the organic precursors was to strengthen the adhesion both among the nanostructures of the functional material itself and between the sensing layer and the alumina substrate. The resulting pastes were treated by sonication and screen-printed onto alumina substrates (2.54 × 2.54 mm^2). The semiconducting MOX films (1 mm^2) were sintered in air for 3 h at 450 °C to remove the organic binder and improve mechanical stability. The substrates were equipped with interdigitated gold contacts on the front side, to provide the bias current for measuring the resistance of the sensitive film, and with a platinum heater on the back side, to thermally activate the sensing material at its optimal working temperature. The alumina substrates were bonded to a standard TO-39 support through thermo-compression of 60 μm diameter gold wires.[19]

5.2 Characterization of functional materials

To investigate the correlation between gas-sensing performance and surface properties of In_2O_3-based films, three approaches were exploited.

5.2.1 Electrical characterization *vs.* CO_2. Experimentation in a standard test chamber for identifying optimal working temperature, sensitivity, response and recovery times, humidity influence, selectivity, cross-selectivity, and stability.

5.2.2 Catalytic sites. Identification of the strength of the active sites, present at the surface level, and their affinity for the target gas. In particular, the functionalized nanostructured powders were heated at 150 and 300 °C in presence of CO_2, to evaluate the presence of basic sites over the surface.

5.2.3 *Operando* DRIFT investigation. This study focuses on the exploration of the sensing mechanism and the formation of intermediate species over the surface of In_2O_3-based sensors and powders when exposed to the analyte. For this purpose, the sensors were thermo-activated at their operational temperature while a spectroscopy analysis was carried out under both dry and humid conditions.

5.3 Electrical characterization setup

The sensors were electrically characterized using an experimental setup and specific schematization detailed in.[6,19] In particular, the sensors were tested in a 622 cm^3 gas-flow sealed chamber. Synthetic air (20% O_2 and 80% N_2) and target gases from certified cylinders (N5.0 degree of purity, SAPIO) were mixed and fluxed through mass-flow controllers at 500 standard cubic centimetres per minute (sccm). The filling time of the test chamber was calculated to be about 1 min and 15 s, as it depends on the size, the geometry of the chamber, and the velocity of the gas flow. A commercial Honeywell HIH-4000 humidity sensor was used to monitor the temperature and relative humidity within the test chamber. A portion of the overall flux (air) was fluxed *via* a bubbler filled with distilled water to achieve the moist conditions.

Considering the *n*-type behaviour of indium oxide, the gas-response (R) was calculated according eqn (3), where G_{air} and G_{gas} are the conductance in dry air and the conductance under target-gas exposure, respectively.

$$R = \begin{cases} \dfrac{(G_{gas} - G_{baseline})}{G_{baseline}} \text{ for reducing gas} \\ \dfrac{(G_{baseline} - G_{gas})}{G_{gas}} \text{ for oxidizing gas} \end{cases} \quad (3)$$

5.3.1 Working temperature. Optimal working temperature of the sensors was determined by measuring the conductance change before and after injection of 1000 ppm of CO_2 in the dry carrier within 150–300 °C.

5.3.2 Sensitivity. To evaluate the sensitivity *vs.* CO_2, Na-doped and pure sensors were exposed to different analyte concentrations within 250–5000 ppm, a range of interest for both indoor and outdoor applications. For the former, 5000 ppm is the Threshold Limit Value (TLV).[27]

5.3.3 Humidity effect. The influence of humidity on the sensing performance *vs.* CO_2 was investigated at midrange (1200 ppm) *vs.* increasing concentrations of water vapor starting from 2 to 70 relative humidity (RH%).

5.3.4 Selectivity. To assess real-world applicability, film selectivity was recorded in presence of common interferents, such as ethanol, toluene, NO_2, and CO, at various concentrations. These gases were chosen based on their relevance to indoor and outdoor air quality, as for National Institute for Occupational Safety and Health (NIOSH) and American Society of Heating, Refrigerating and Air-Conditioning Engineers (ASHRAE) guidelines.[28–30]

5.3.5 Cross-selectivity. The cross-selectivity of the Na-doped sensors towards 1000 ppm of CO_2 in the presence of 1 ppm (baseline) of ethanol was performed in dry and wet conditions (20 RH%). These tests with ethanol, a common Volatile Organic Compound (VOC) and a highly responsive target for MOX sensors, were carried out to establish the material's selectivity towards CO_2 over common reducing gases, demonstrating its suitability for several applications, *e.g.* indoor air quality monitoring.[1]

5.3.6 Stability. The stability test was performed on the most promising sensor by exposing it to 250 ppm for one week.

5.3.7 Response and recovery times. The response (τ_{res}) and the recovery (τ_{rec}) times of the sensors were estimated as the times needed to attain 90% of the steady-state response and

required to switch back to 90% of the baseline value, respectively.[19]

5.4 Catalytic sites investigation

Chemisorption analyses carried out by a custom-made Chemisorb analyser, available at Università Ca' Foscari in Venezia.[31,32] The surface basicity and acidity of the materials were assessed *via* TPD with probe molecules such as CO_2 and NH_3, respectively. The resulting desorption profiles allowed for the precise determination of the site's strength (differentiated by their desorption temperature). Furthermore, TPR experiments were conducted to evaluate the reducibility of the oxide and the presence of labile oxygen species, a key factor influencing the material's activity and sensing mechanism. This comprehensive approach allowed for a complete understanding of the material's surface properties.

For TPD analyses with CO_2, the powders were desiccated in an oven at 110 °C overnight in dry air to desorb humidity then cooled down to room temperature. Then, 50 mg of powder was introduced into a quartz reactor and pretreated in CO_2 atmosphere (30 mL min^{-1}) at 150 and 300 °C for 1 hour. After cooling, programmed heating at 10 °C min^{-1} to 900 °C in He flow was carried out, monitoring CO_2 desorption by thermoconductivity detector (TCD).

Prior to TPD analysis with ammonia (NH_3), samples were dried overnight at 110 °C. Next, 50 mg were introduced into a quartz reactor and treated in a He atmosphere (40 mL min^{-1}) at 25 and 300 °C for 1 hour. After cooling, the sample was exposed to 5% NH_3 mixture in helium for 30 min at the same temperatures (25 and 300 °C). A trap of sulfuric acid (H_2SO_4) was placed at the reactor outlet to complex the ammonia. Finally, programmed heating was carried out at 10 °C min^{-1} to 900 °C in He flow, monitoring NH_3 desorption by TCD.

TPR experiments were carried out in a lab-made apparatus with 5% H_2/Ar gas mixture (40 mL min^{-1}). H_2 uptake was monitored by a Gow-Mac TCD. 100 mg of the sample were loaded in a quartz reactor and flushed with a mixture of H_2 (5%)/Ar from 25 to 900 °C, with a rate of 10 °C min^{-1}.

5.5 *Operando* DRIFT setup

The kinetics at the gas–solid interface was elucidated through *operando* DRIFT experiments utilizing a Bruker Vertex 70v vacuum FTIR spectrometer equipped with a Praying Mantis accessory. In parallel, the electrical characterization of In_2O_3-based sensors was performed by using a dedicated apparatus, including a customized sealed gas test chamber with a void volume of 0.5 cm^3 and a data acquisition system, namely Zefiro (Java software). The test chamber's filling time was calculated at approximately less than 1 s. Complete details regarding the experimental setup are provided in previous works.[33,34]

5.5 1 DRIFT measurements. Single-channel spectrum is related to the absorption caused by functional groups of chemical species adsorbed on the surface and by outermost atoms of the sensing material. The spectra were acquired through a liquid nitrogen-cooled mercury cadmium tellurium mid-band detector, with a spectral range from 800 to 4000 cm^{-1}. Absorbance spectra (AB) were calculated by using the following equation:[6,35]

$$\mathrm{AB}\ (\lambda) = -\log_{10} \frac{I_{\mathrm{sample}\ (\lambda)}}{I_{\mathrm{background}\ (\lambda)}} \quad (4)$$

where $I_{\mathrm{sample}\ (\lambda)}$ and $I_{\mathrm{background}\ (\lambda)}$ are the sample and background spectra, respectively. Each spectrum was collected at a resolution of 4 cm^{-1}, averaging 1024 scans with a beam spot size of 2.5 mm. All the optical bench settings and spectral data acquisition were performed through Bruker OPUS software.

5.5.2 Characterization of the sensing films: *operando* measurements. Before CO_2 exposure, the measuring chamber was kept in a constant flow of 100 sccm of dry air, while the sensor operating temperature was gradually increased with steps of 50 °C up to 250 °C. Each temperature step was kept for as long as needed to allow thermodynamic stabilization of the surface. Surface reactivity of the sensor was evaluated after maintaining the device at 250 °C for 1 day under a 100 sccm constant flow of synthetic dry air and an applied voltage between the electrodes of 1.0 V. Then, we evaluated the spectral background for each reported measurement. After baseline stabilization for a few hours, the device was exposed to a mixture of 1000 ppm of CO_2 and synthetic air under dry ($\approx$1% RH at 30 °C) and wet conditions (up to 22 RH% at 30 °C).

5.5.3 Characterization of the sensing powders: *in-situ* measurements. To effectively study the physico-chemical adsorption processes at the In_2O_3-gas interface, further *in-situ* DRIFT measurements were conducted on both pure and doped powders at 250 °C in dry and wet conditions. These samples were carefully housed in a custom-made crucible, designed to fit the specific geometry of the test chamber.[35] *In-situ* powder DRIFTS technique used a larger sample holder (area 78.5 mm^2) than the sensing films (area 2.11 mm^2). Owing to the limited sensing area of the film, a 2.5 mm IR spot diameter was used for those measurements, while the bigger powder holder permitted the utilization of a 4 mm IR spot diameter. Therefore, a greater IR spot results in a significant boost in overall signal intensity and instrument sensitivity.

Author contributions

A. R. conceptualized the core idea, established the overall direction of the study, and prepared the original draft manuscript, including primary data visualization and curation; A. R. was responsible for all material synthesis procedures and performed all detailed electrical and DRIFT spectroscopy measurements; A. G., A. P. and L. V. conducted and curated the XPS analyses; M. F. performed TEM and HR-TEM and SEM/EDX analyses; M. A. carried out the XRD measurement and data analysis; G. V. contributed to BET surface area measurements; TPD and TPR measurements and data analyses interpretation were conducted by E. G. and M. S.; R. T. perfomed ICP-MS analysis and data interpretation; B. F. and V. G. contributed to supervision and editing. All authors critically revised the manuscript, contributed to its refinement, and approved the final version for submission.

Conflicts of interest

The authors declare no conflict of interest.

Data availability

The supporting data and experimental information for this article have been included in the supplementary information (SI). Supplementary information is available. See DOI: https://doi.org/10.1039/d5ta08957c.

Acknowledgements

This work was funded (POR FSE 2014/2020) by Regione Emilia-Romagna. Research Project for Technology Transfer and Business. Integrated management of satellite data and ground IoT sensors aimed at sustainability in precision farming practices for regional crops of excellence.

References

1 M. Magoni, A. Rossi, F. Tralli, P. Bernardoni, B. Fabbri, A. Gaiardo, S. Gherardi and V. Guidi, *ACS Sens.*, 2024, **9**, 2999.
2 M. De Jode, *Indoor Environ.*, 2024, **1**, 100030.
3 R. Maddalena, M. J. Mendell, K. Eliseeva, W. R. Chan, D. P. Sullivan, M. Russell, U. Satish and W. J. Fisk, *Indoor Air*, 2015, **25**, 362.
4 Y. Ughade, S. Mehta, G. Patel, R. Gowda, N. Joshi and R. Patel, *Micromachines*, 2025, **16**, 466.
5 J. Wang, G. Zhang, J. Zhu, X. Zhang, F. Ding, A. Zhang, X. Guo and C. Song, *ACS Catal.*, 2021, **11**, 1406.
6 A. Rossi, B. Fabbri, E. Spagnoli, A. Gaiardo, M. Valt, M. Ferroni, M. Ardit, S. Krik, A. Pedrielli, L. Vanzetti and V. Guidi, *ACS Appl. Mater. Interfaces*, 2023, **15**, 33732.
7 K. Bhattacharyya, A. Danon, B. K. Vijayan, K. A. Gray, P. C. Stair and E. Weitz, *J. Phys. Chem. C*, 2013, **117**, 12661.
8 E.-M. Köck, M. Kogler, T. Bielz, B. Klötzer and S. Penner, *J. Phys. Chem. C*, 2013, **117**, 17666.
9 T. Suzuki, A. Sackmann, A. Oprea, U. Weimar and N. Bârsan, *ACS Sens.*, 2020, **5**, 2555.
10 X. Wang, A. Rendón-Patiño, J. M. R. Gallo, D. Mateo and J. Gascon, *J. Mater. Chem. A*, 2024, **12**, 23541.
11 A. Marikutsa, A. Novikova, M. Rumyantseva, N. Khmelevsky and A. Gaskov, *Sens. Actuators, B*, 2021, **326**, 128980.
12 R. D. Shannon, *Acta Crystallogr., Sect. A*, 1976, **32**, 751.
13 ISO [International Organization for Standardization], *Determination of the specific surface area of solids by gas adsorption - BET method (ISO 9277:2022)*, Ref. Number ISO. 9277, 2022, https://www.iso.org/standard/71014.html.
14 K. Pokrovski, K. T. Jung and A. T. Bell, *Langmuir*, 2001, **17**, 4297.
15 P. H. Ho, G. Tizzanini, S. Ghosh, W. Di, J. Shao, O. Pajalic, L. Josefsson, P. Benito, D. Creaser and L. Olsson, *Energy Fuels*, 2024, **38**, 5407.
16 X. Gao, Z. Wang, Q. Huang, M. Jiang, S. Askari, N. Dewangan and S. Kawi, *Catal. Today*, 2022, **402**, 88.
17 D. Degler, B. Junker, F. Allmendinger, U. Weimar and N. Barsan, *ACS Sens.*, 2020, **5**, 3207.
18 R. G. Pavelko, H. Daly, M. Hübner, C. Hardacre and E. Llobet, *J. Phys. Chem. C*, 2013, **117**, 4158.
19 A. Rossi, E. Spagnoli, A. Visonà, D. Ahmed, M. Marzocchi, V. Guidi and B. Fabbri, *Chemosensors*, 2024, **12**, 111.
20 C. A. Zito, T. M. Perfecto, A.-C. Dippel, D. P. Volanti and D. Koziej, *ACS Appl. Mater. Interfaces*, 2020, **12**, 17745.
21 K. Fan, H. Qin, L. Wang, L. Ju and J. Hu, *Sens. Actuators, B*, 2013, **177**, 265.
22 K. Grossmann, R. G. Pavelko, N. Barsan and U. Weimar, *Sens. Actuators, B*, 2012, **166–167**, 787.
23 I. Can, U. Weimar and N. Barsan, in *Proceedings of Eurosensors 2017, Paris, France, 3–6 September 2017*, MDPI, 2017, pp. 432.
24 N. Barsan, D. Koziej and U. Weimar, *Sens. Actuators, B*, 2007, **121**, 18.
25 A. Gurlo, *ChemPhysChem*, 2006, **7**, 2041.
26 A. Álvarez, M. Borges, J. J. Corral-Pérez, J. G. Olcina, L. Hu, D. Cornu, R. Huang, D. Stoian and A. Urakawa, *ChemPhysChem*, 2017, **18**, 3135.
27 https://www.acgih.org/carbon-dioxide/.
28 J. G. Allen, P. MacNaughton, U. Satish, S. Santanam, J. Vallarino and J. D. Spengler, *Environ. Health Perspect.*, 2016, **124**, 805.
29 S. C. Lee and M. Chang, *Indoor Air*, 1999, **9**, 134.
30 A. U. Raysoni, T. H. Stock, J. A. Sarnat, M. C. Chavez, S. E. Sarnat, T. Montoya, F. Holguin and W.-W. Li, *Environ. Pollut.*, 2017, **231**, 681.
31 C. Pizzolitto, F. Menegazzo, E. Ghedini, G. Innocenti, A. Di Michele, M. Mattarelli, G. Cruciani, F. Cavani and M. Signoretto, *ACS Sustainable Chem. Eng.*, 2020, 0c02373.
32 F. Pinna, M. Signoretto, G. Strukul, S. Polizzi and N. Pernicone, *React. Kinet. Catal. Lett.*, 1997, **60**, 9.
33 M. Della Ciana, M. Valt, B. Fabbri, P. Bernardoni, V. Guidi and V. Morandi, *Rev. Sci. Instrum.*, 2021, **92**, 074702.
34 M. Valt, M. D. Ciana, B. Fabbri, D. Sali, A. Gaiardo and V. Guidi, *Sens. Actuators, B*, 2021, **341**, 130012.
35 E. Tavaglione, E. Spagnoli, M. Valt, P. Bernardoni, M. Della Ciana, F. Bottegoni, M. Negri, F. Scali, C. Zucchetti, M. Ferroni, M. Ardit, L. Vanzetti, V. Cristino, F. Di Benedetto and B. Fabbri, *Sens. Actuators, B*, 2025, **444**, 138504.